**Chapter-4**

# QUASILINEAR ANALYSIS OF SHEATH PLASMA INSTABILITY IN INVERTED FIREBALLS

***Abstract:*** *The sheath plasma instabilities (SPIs) are excitable inside unstable inverted fireball (IFB) systems under adequate circumstances. They are theoretically analysed in this chapter using the quasilinear framework of relevant laboratory scales. The applied bifluidic plasma model yields charge specific governing equations corresponding to electrons and ions. These individual fluid equations are systematically rearranged in terms of density and electrostatic potential and substituted in the Poisson equation. The Poisson equation upon solved numerically and applying the boundary conditions generates the quasilinear expressions of the dependent plasma parameters. These plasma parameters comprise of electron (ion) density, velocity, electrostatic potential, and electric field. The 2-D pictorial illustration of these parameters points at their peakonic and bifold-solitonic (mirror-solitonic) nature*[†]*. The 4-D colormaps also validate the 2-D profiles as anticipated. The induced electric field is observed to manifest similar experimentally reported evanescent behaviour. This emboldens the reliability of the bifluidic quasilinear IFB model formalism used herein. Eventually, the practical applicability of SPI study in both pure and applied sciences across the domains are briefly presented.*

## 4.1 INTRODUCTION

Formation of a sheath is an imminent outcome of plasma-electrode interaction (PEI). A stable sheath is responsible for greater plasma stability; however, a spatiotemporally fluctuating sheath may also lead to certain plasma instabilities under special circumstances. A stable plasma sheath constrains the electric field emanated from the introduced electrode within its span, freeing the ambient plasma from undergoing any field drifted instability. In addition, the sheath formed at the plasma chamber wall also prevents the plasma constituents from escaping through the walls aiding in maintaining quasineutrality across the ambient plasma region. The plasma sheath also possesses a strong nonlinear intrinsic electric field arising due to space charge polarization across it against the electric field strength of the externally biased electrode in the plasma setup [1].

[†]Dutta, S. and Karmakar, P. K. Sheath plasma instability in inverted fireballs, *Chaos, Solit. & Fract*., 186(115259):1-12, 2024.

The PEI can also trigger several instabilities. Some of the commonly observed instabilities in the laboratory plasma fireball (FB) system are the two-stream instability (TSI), the Kelvin-Helmholtz instability (KHI), the ion-acoustic instability (IAI), the secondary-ionization instability (SII), the sheath plasma instability (SPI), and so on [2-4]. Among the following instabilities, the ubiquitous SPI is theoretically analyzed herein using a bifluidic plasma model approach with the help of a quasilinear (first-order nonlinearity) perturbation formalism in laboratory plasma scales. The derived parameters during the SPI excitation within an inverted fireball (IFB) comprise of quasilinear variation of the electron (ion) density, velocity, sheath electrostatic potential, and electric field.

The SPI can excite across a sheath region formed around (for regular FB) or within (for IFB) a positively biased electrode submerged in Maxwellian plasma. This instability is an outcome of the nonzero electron inertia, driven by the negative radiofrequency (RF) sheath resistance, and it manifests a maximum amplitude at the sheath plasma resonance (SPR) frequency ($\omega \leq \omega_{pe}$). The negative RF sheath resistance results into a maximum of the electron current ($I$) and charge fluid velocity ($v_{e(i)}$) at the minima of the corresponding electrostatic potential ($\phi$), and vice-versa, across the sheath region. Hence, a phase difference of 180° is noticed to exist in between the two electric parameters ($I$ and $\phi$), as they evolve against each other towards their respective maximum [4].

The harmonics of the instability are observed to radiate from the central electrode as EM waves. The central electrode behaves like an antenna. The oscillating ions adjacent to the sheath edge may grow into some burst-like rf emissions also [4]. It may be noted that one of the outcomes of the SPI is the ionization of the neutrals across the sheath region. The liberated electrons reduce the space charge density and electric field strength, finally ceasing the SPI. But, due to the consistent external biasing of the introduced anode the SPI starts over [5]. The outcome of the SPI is observed in terms of various plasma parameters involved. The quasilinear analysis of these physical parameters through a bifluidic plasma model yields fluctuation results which corroborate with the experimental ones reported in the literature [6]. Against this backdrop, a necessary brief overview is presented herein to illuminate the adopted quasilinear framework in the bifluidic plasma model approach.

Introducing a small amplitude perturbation in a plasma system can trigger linear variation of the perturbed plasma parameters, where the rate of change of the perturbed plasma parameters is directly proportional to their instantaneous magnitudes of perturbation. This earliest stage of instability is to be analyzed linearly because of the small-

scale perturbation. However, the instability does not manifest a variation exactly proportional to their first-order perturbed instantaneous magnitudes in the consecutive stages [7]. Therefore, a quasilinear stage of the instability sets in subsequently. This stage of the instability is believed to be well illuminated and understood in the framework of quasilinear formalism. This quasilinear treatment is applicable to the plasma systems when the collective oscillation energy of the constitutive plasma particles is less than the effective thermal energy, but greater than the background noise energy preexisting naturalistically in the system [8]. There is a weak turbulence in the medium without strong correlation between the linear waves due to this small order of nonlinearity.

In contrast, the presence of diverse parametric correlations makes the system purely nonlinear in nature. The ionic constituents start to participate in the instability dynamics but are still in considerably low magnitude compared to the electrons. The fluid convection (nonlinear) and dispersion (linear) conjointly yield to the quasilinear stage where both the linear and nonlinear natures can be partially observed across the plasma parameters [9]. Hence, the quasilinear stage is a transient phase bridging across the linear and nonlinear phases of instability. This quasilinear treatment is more general in comparison to the special linear treatment of the plasma system, and it smoothly recreates the experimentally observed SPI driven outcomes reported in the literature with substantial accuracy [10].

Having briefly discussed the adopted quasilinear framework, the relevance of the SPI study is emphasized hereafter. The knowledge of SPI is very important in interpreting antenna signals received from charged spacecraft since it resembles that of the plasma fireball sheath (PFBS) system formed in a laboratory plasma chamber. The antenna (in astrospace plasmas) or probe (in laboratory plasmas) get encapsulated with plasma sheaths. The EM wave or signal transmitted from the sheath encapsulated transmitters (probe or antenna) may differ from the actual signal with added disturbance due to the excited SPI. The same applies to the electrodynamic tethers also, as the tether wire gets electrically charged (behaves as an electrode) with the inevitable sheath formation around it while moving across the astroplasmic medium [4]. The variation of the electrostatic potential across the tether wire excites the SPI. It hinders natural signal transmission. Besides, the same sheath property (of undergoing SPI) can be used in the MW resonators to produce MW radiation to be utilized in diverse other experiments [4, 5].

The quasilinear analysis of the SPI excited in a PFS system with a defined spherical IFB geometry as developed in this chapter is the first of its kind as far as known in the

literature. The novelty of this quasilinear SPI analysis lies in the development of a unique construct of an ODE(2) (on the quasilinear electrostatic potential ($\phi_1$)), decoupled out of the closed set of the basic SPI governing equations, used for describing the fluctuation dynamics under consideration. A numerical analysis is carried out to obtain its exact solutions with peakonic and bifold-solitonic (mirrored-solitonic) nature after imposing the necessary boundary conditions applicable in the model. The spatial variations of the derived plasma parameters manifest the actual behavior of the plasma IFB undergoing the SPI. It ends up with realistic implications and applications in diversified fields.

## 4.2 PHYSICAL MODEL AND FORMALISM

The SPI is assumed to excite inside a hollow and meshed IFB anode of spherical geometry. The surrounding plasma is considered to be bifluidic in nature with individual electronic and ionic species collectively contributing to the SPI dynamics. The presence of neutrals is limited to ignorable amount. The spherical geometry is experienced to be most convenient for both experimental IFB creation and its theoretical modelling [9]. In theoretical modelling, it helps in minimizing the complications inextricably linked to the polar and azimuthal components [11]. Therefore the 3-D system is logically simplified to a 1-D problem with only radial variation without hindering the generality of the model set-up. The individual fluid dynamics of electrons and ions are governed by their respective set of two governing equations, viz., the electron (ion) continuity equation and momentum equation. The final closure is obtained by the common Poisson equation, which encompasses both electron and ion dynamics. The density inhomogeneity developed during the SPI excitation yields a nonzero RHS and charge specific perturbed density parameters for individual electrons and ions.

It must be added that the SPI excitation triggers both spatial and temporal variation of the perturbed plasma parameters [4, 5]. However, due to the asymptotic observation of them, the expressions are explicitly noticed to be specifically spatially invariant. This expedites the SPI analysis against any instantaneous parametric variations. The asymptotic study forms a steady-state (time-stationary) theoretical IFB model without the loss of any generality of SPI dynamics. Besides, no plasma existential conditions ($(r, t) \gg (\lambda_D, \omega_p^{-1})$) are violated during the SPI study further emboldening the current research.

As explained above, we are interested in the quasilinear SPI analysis through substitution of the perturbed plasma parameters against their hydrostatic homogeneous

equilibrium values. The set of unnormalized governing equations explaining the individual electron (ion) dynamics in spherical polar coordinates are cast as

$$\partial_t n_{e(i)} + \left(\frac{1}{r^2}\right)\partial_r\left(r^2 n_{e(i)} v_{e(i)}\right) = 0, \tag{4.1}$$

$$m_{e(i)} n_{e(i)}\left[\partial_t v_{e(i)} + v_{e(i)}\partial_r v_{e(i)}\right] = -\partial_r(k_B T_{e(i)} n_{e(i)}) \pm e n_{e(i)}(-\partial_r \phi) +$$
$$\partial_r\left[\eta\left(\frac{1}{r^2}\right)\left(r^2\partial_r v_{e(i)}\right)\right] + \partial_r\left[\left(\xi + \frac{\eta}{3}\right)\left(\frac{1}{r^2}\partial_r\left(r^2 v_{e(i)}\right)\right)\right] + \left(\frac{e^2 n_{e(i)}}{4\pi\epsilon_o}\right)^2\left[\frac{\pi^2 m_e}{(k_B T_e)^3}\right]^{\frac{1}{2}} v_{e(i)}. \tag{4.2}$$

Here, Eq. (4.1)-(4.2) denotes the continuity and momentum equation of electrons (ions). The various linear differential operators used in these equations are symbolized as $\partial_t = \partial/\partial t$, $\partial_r = \partial/\partial r$ and so on. Besides, the terms $n_{e(i)}$, $v_{e(i)}$, $m_{e(i)}$, and $T_{e(i)}$ denote the electron (ion) charge number density, velocity, mass, and temperature, respectively. The rest of the parameters, such as $P$, $\phi$, $\eta$, $\xi$, and $e$ denote the thermal pressure, electrostatic potential, coefficient of shear viscosity, coefficient of bulk viscosity, and electronic charge, respectively. In addition, the thermal pressure ($P$) and momentum imparted due to intercomponent charged particle collision are given by $n_{e(i)}k_B T_{e(i)}$ and $\left(e^2 n_{e(i)}/4\pi\epsilon_o\right)^2[\pi^2 m_e/(k_B T_e)^3]^{1/2}$ [7], respectively.

The individual electron and ion dynamics are coupled into a single equation for final solution by substituting corresponding number densities on the RHS of the Poisson equation. It depicts the spatial potential variation in terms of inhomogeneity of charge number density, given as

$$r^{-2}\partial_r(r^2\partial_r\phi) = 4\pi e(n_e - n_i). \tag{4.3}$$

Evidently, Eq. (4.3) representing the Poisson equation illustrates the spatially varying nonzero electrostatic potential across the IFB sheath which leads to SPI excitation as discussed before.

Since, we are interested in the steady-state SPI evolution ($\partial_t \sim 0$, and $\partial_r \neq 0$) in the IFB system, we ignore all the temporally varying terms throughout the governing equations (Eqs. (4.1)-(4.2)). Their corresponding time-stationary forms are respectively given as

$$n_{e(i)}\partial_r v_{e(i)} + v_{e(i)}\partial_r n_{e(i)} + \left(\frac{2}{r}\right) n_{e(i)} v_{e(i)} = 0, \tag{4.4}$$

$$k_B T_e \partial_r n_{e(i)} = \pm e n_{e(i)}(-\partial_r \phi) + \partial_r \left[\xi \left(\partial_r v_{e(i)} + \left(\frac{2}{r}\right) v_{e(i)}\right)\right] + p_o n_{e(i)}^2 v_{e(i)}. \tag{4.5}$$

Since, the plasmic fluid motion is unidirectional (radial), we ignore the coefficient of bulk viscosity ($\eta = 0$) term (Eq. (4.2)) in Eq. (4.5). Besides, the term $\left(e^2 n_{e(i)}/4\pi\epsilon_o\right)^2 [\pi^2 m_e/(k_B T_e)^3]^{1/2}$ is replaced with $p_o n_{e(i)}^2$ in Eq. (4.5). It must also be added that due to charge number density ($n_{e(i)}$) across the FB, the bulk viscosity ($\xi$) is not radially invariant, but proportionally varying with respect to $n_{e(i)}$ given as [12]

$$\xi = \frac{5}{3} k_B T_e \left(\frac{n_{e(i)}}{v_{e(i)}}\right), \tag{4.6}$$

We replace $\xi$ from Eq. (4.6) in Eq. (4.5), resulting in

$$k_B T_e \partial_r n_{e(i)} = \pm e n_{e(i)}(-\partial_r \phi) + \left(\frac{5}{3} k_B T_e\right) \partial_r \left[\left(\frac{n_{e(i)}}{v_{e(i)}}\right) \partial_r v_{e(i)} + \left(\frac{2}{r}\right) n_{e(i)}\right] + p_o n_{e(i)}^2 v_{e(i)}, \tag{4.7}$$

The simplified (expanded) Poisson equation may be written as

$$\partial_r^2 \phi + \left(\frac{2}{r}\right) \partial_r \phi = 4\pi e(n_e - n_i). \tag{4.8}$$

The linear differential operator used in Eq. (4.8) is $\partial_r^2 = \partial^2/\partial r^2$. For the instability analysis, the plasma parameters ($F_\alpha(r)$) are allowed to undergo perturbation about their hydrostatic homogeneous equilibrium values ($F_o(r)$) with the $\epsilon$-expanded form cast as

$$F_\alpha(r) = F_o + \sum_{\alpha=1}^{\infty} \epsilon^\alpha F_\alpha(r), \tag{4.9}$$

$$F(r) = [n_e \quad v_e \quad n_i \quad v_i \quad \phi]^T, \tag{4.10}$$

$$F_o(r) = [n_{eo} \quad 0 \quad n_{io} \quad 0 \quad 0], \tag{4.11}$$

$$F_\alpha(r) = [n_{e\alpha} \quad v_{e\alpha} \quad n_{i\alpha} \quad v_{i\alpha} \quad \phi_\alpha]^T. \tag{4.12}$$

The symbol $\epsilon$ denotes an order parameter signifying the balanced strength of nonlinearity and dispersion. Its power ($\alpha$) of magnitude unity ($\alpha = 1$) in the perturbed expressions denotes quasilinear (first-order nonlinear) treatment applied herein. This treatment differs from the linear perturbation theory on the grounds that the lowest-order fluctuations are also modified with $\epsilon$ as fluctuation amplitude. Similarly, it differs from a purely nonlinear analysis because the higher-order terms resulting from the $\epsilon$-expansion are summarily ignored. Besides, quasilinearity is the smallest-order nonlinearity at which the rate of change of a plasma parameter ($dF/d(r,t)$) is not directly proportional to its concurrent magnitude ($F(r,t)$). Applying the defined perturbation scheme, as shown in Eqs. (4.9)-(4.12), the linearized forms of Eq. (4.4), Eq. (4.7), and Eq. (4.8) for our quasilinear treatment ($\epsilon$-dictated) can be respectively written as

$$n_{e(i)o}\partial_r v_{e(i)1} + v_{e(i)1}\partial_r n_{e(i)o} + \left(\frac{2}{r}\right) n_{e(i)o} v_{e(i)1} = 0, \tag{4.13}$$

$$k_B T_e \partial_r n_{e(i)1} = \left(\frac{5}{3} k_B T_e\right) \partial_r \left[\left(\frac{n_{e(i)o}}{v_{e(i)1}}\right) \partial_r v_{e(i)1} + \left(\frac{n_{e(i)1}}{v_{e(i)o}}\right) \partial_r v_{e(i)o} + \left(\frac{2}{r}\right) n_{e(i)1}\right] + p_o n_{e(i)o}^2 v_{e(i)1} \pm e n_{e(i)o}(-\partial_r \phi_1), \tag{4.14}$$

$$\partial_r^2 \phi_1 + \left(\frac{2}{r}\right) \phi_1 = 4\pi e(n_{e1} - n_{i1}). \tag{4.15}$$

The equilibrium (unperturbed) electron (ion) number density is experimentally noticed to have a Gaussian nature given as $n_{e(i)o} = n_o = n_c \exp(-\gamma r^2)$ [13]. It should be noted that two of the terms in Eq. (4.14) viz. $\left(n_{e(i)o}/v_{e(i)1}\right)\partial_r v_{e(i)1}$ and $\left(n_{e(i)1}/v_{e(i)o}\right)\partial_r v_{e(i)o}$ are not quasilinear (first-order) in nature as the first term reduces to the zeroth-order and the second term is undefined (with denominator $v_{e(i)o} = 0$). Ignoring such inadmissible terms in Eq. (4.14) and substituting for $n_{e(i)o}$ in Eqs. (4.13)-(4.14), we have

$$n_c \exp(-\gamma r^2)\partial_r v_{e(i)1} + v_{e(i)1} n_c(-2\gamma r)\exp(-\gamma r^2) + \left(\frac{2}{r}\right) n_c \exp(-\gamma r^2) v_{e(i)1} = 0, \tag{4.16}$$

Simplifying Eq. (4.16), we have

$$\partial_r v_{e(i)1} = \left(2\gamma r - \frac{2}{r}\right) v_{e(i)1}, \tag{4.17}$$

Integrating Eq. (4.17) indefinitely, we have

$$v_{e(i)1} = \frac{v_{e(i)c}}{r^2} \exp(\gamma r^2). \tag{4.18}$$

For the electron and ion dynamics, the individual quasilinear velocity expressions are respectively given as

$$v_{e1} = \frac{v_{ec}}{r^2} \exp(\gamma r^2), \tag{4.19}$$

$$v_{i1} = \frac{v_{ic}}{r^2} \exp(\gamma r^2). \tag{4.20}$$

Here, $v_{ec}$ and $v_{ic}$ are the integration constants, denoting the strength of the quasilinear velocity perturbations in the electron and ion dynamics at the IFB center ($r = 0$), respectively.

Now, repeating the same with Eq. (4.14), we have

$$k_B T_e \partial_r n_{e(i)1} = \frac{10}{3} k_B T_e \partial_r \left(\left(\frac{1}{r}\right) n_{e(i)1}\right) + p_o n_c^2 \exp(-2\gamma r^2)\, v_{e(i)1} \mp e n_c \exp(-\gamma r^2)(\partial_r \phi_1), \tag{4.21}$$

Simplifying Eq. (4.21) with substitution of $v_{e(i)1}$ from Eq. (4.18) and rearranging the terms, we have

$$\partial_r n_{e(i)1} = \mp \left(\frac{e n_c}{k_B T_e}\right) \exp(-\gamma r^2)\, \partial_r \phi_1 + \left(\frac{p_o n_c^2}{k_B T_e}\right) \frac{v_{e(i)c}}{r^2} \exp(-\gamma r^2) + \frac{10}{3} \partial_r \left(\frac{1}{r} n_{e(i)1}\right), \tag{4.22}$$

Integrating Eq. (4.22) indefinitely with respect to $r$ using MATLAB, we have

$$n_{e(i)1} = \mp \left(\frac{e n_c}{k_B T_e}\right) \left[\exp(-\gamma r^2)\, \phi_1 + \frac{1}{2}\sqrt{\frac{\pi}{\gamma}}\, \partial_r \phi_1\right]$$

$$+\left(\frac{p_o n_c^2}{k_B T_e}\right) v_{e(i)c}\left(-\frac{1}{r}-\gamma r+\frac{\gamma^2 r^3}{3!}+\cdots\right)+\frac{10}{3}\left(\frac{1}{r}\right) n_{e(i)1}+n_{e(i)a}. \quad (4.23)$$

Here, $n_{e(i)a}$ is a new integration constant denoting the quasilinear charge number density perturbation at infinity (ambient plasma). Asymptotically, $n_{e(i)a}=0$ at $r\to\infty$, since the SPI is dominant only inside the IFB. Thus, removing $n_{e(i)a}$, and using the boundary condition of $n_{e(i)}(r\to\infty)=0$, we have

$$n_{e(i)1}=\mp\left(\frac{3r}{3r-10}\right)\left(\frac{en_c}{k_B T_e}\right)\left[\exp(-\gamma r^2)\,\phi_1+\frac{1}{2}\sqrt{\frac{\pi}{\gamma}}\,\partial_r\phi_1\right]-\left(\frac{p_o n_c^2 v_{e(i)c}}{k_B T_e}\right)\frac{1}{r}\left(\frac{3r}{3r-10}\right). \quad (4.24)$$

It may be noted here that for the IFBs with larger dimensions yielding $3r\geq 10$, the individual charge number density perturbation equations for the electrons and ions, respectively read as

$$n_{e1}=-\left(\frac{3r}{3r-10}\right)\left(\frac{en_c}{k_B T_e}\right)\left[\exp(-\gamma r^2)\,\phi_1+\frac{1}{2}\sqrt{\frac{\pi}{\gamma}}\,\partial_r\phi_1\right]-\left(\frac{p_o n_c^2 v_{ec}}{k_B T_e}\right)\frac{1}{r}\left(\frac{3r}{3r-10}\right); \quad (4.25)$$

$$n_{i1}=\left(\frac{3r}{3r-10}\right)\left(\frac{en_c}{k_B T_e}\right)\left[\exp(-\gamma r^2)\,\phi_1+\frac{1}{2}\sqrt{\frac{\pi}{\gamma}}\,\partial_r\phi_1\right]-\left(\frac{p_o n_c^2 v_{ic}}{k_B T_e}\right)\frac{1}{r}\left(\frac{3r}{3r-10}\right). \quad (4.26)$$

However, the typical experimental IFB radius is just $10$ cm at the maximum [13], hence $r\approx 0.1$ m yields $3r/(3r-10)\approx -3r/10$. Using this approximation in Eq. (4.24) and simplifying further, we have

$$n_{e(i)1}=\pm\left(\frac{en_c}{k_B T_e}\right)\left(\frac{3r}{10}\right)\left[\exp(-\gamma r^2)\,\phi_1+\frac{1}{2}\sqrt{\frac{\pi}{\gamma}}\,\partial_r\phi_1\right]+\frac{3p_o n_c^2 v_{e(i)c}}{10k_B T_e}. \quad (4.27)$$

Then, Eq. (4.27) accounts for both the electron and ion dynamics with different suffixes ('$e$' and '$i$') and signs ('+' and '−'), respectively. The separated quasilinear density perturbation expressions from Eq. (4.27) for electron and ion dynamics are respectively given as

$$n_{e1}=\left(\frac{en_c}{k_B T_e}\right)\left(\frac{3r}{10}\right)\left[\exp(-\gamma r^2)\,\phi_1+\frac{1}{2}\sqrt{\frac{\pi}{\gamma}}\,\partial_r\phi_1\right]+\frac{3p_o n_c^2 v_{ec}}{10k_B T_e}, \quad (4.28)$$

$$n_{i1} = -\left(\frac{en_c}{k_B T_e}\right)\left(\frac{3r}{10}\right)\left[\exp(-\gamma r^2)\,\phi_1 + \frac{1}{2}\sqrt{\frac{\pi}{\gamma}}\,\partial_r\phi_1\right] + \frac{3p_o n_c^2 v_{ic}}{10k_B T_e}. \quad (4.29)$$

We substitute Eq. (4.28) and Eq. (4.29) in quasilinear Poisson equation (Eq. (4.15)) to yield

$$\partial_r^2\phi_1 + \left(\frac{2}{r}\right)\partial_r\phi_1 = 4\pi e\left[\frac{6r}{10}\left(\frac{en_c}{k_B T_e}\right)\left(\exp(-\gamma r^2)\,\phi_1 + \frac{1}{2}\sqrt{\frac{\pi}{\gamma}}\,\partial_r\phi_1\right) + \frac{3p_o n_c^2}{10k_B T_e}(v_{ec} - v_{ic})\right]. \quad (4.30)$$

Rearranging Eq. (4.30) and solving it numerically, we have

$$\phi_1(r) = c_1 + \frac{A}{2\gamma^2}\left(\frac{1}{r}\right)\exp(-\gamma r^2) + \frac{Ar}{2\gamma}exp(-\gamma r^2) + \frac{Br^2}{6} - \frac{c_2}{r} - \frac{A\sqrt{\pi}}{4(-\gamma)^{\frac{3}{2}}}erfi(\sqrt{-\gamma}r) + \frac{Ar}{2\gamma}\exp(-\gamma r^2). \quad (4.31)$$

Here, $c_1$ and $c_2$ are integration constants originated in Eq. (4.31), and

$$A = \frac{12\pi e^2 n_c}{5k_B T_e}, \quad (4.32)$$

$$B = \frac{3p_o n_c^2}{10k_B T_e}(v_{ec} - v_{ic}). \quad (4.33)$$

Applying the boundary condition of $\phi_1(r \to \infty) = 0$ in Eq. (4.31), we have

$$\phi_1(r) = \frac{C}{r}\exp(-\gamma r^2) - \frac{c_2}{r}; \quad (4.34)$$

$$C = \frac{A}{2\gamma^2}. \quad (4.35)$$

The numerical values of the involved constants may be assumed in accordance with the experimental observations of electrode potentials reported in the literature [4, 5]. The potential difference between the anode and plasma during the simultaneous excitation of SPR and the SPI are reported to be $\Delta\phi \sim 60$ V [4, 5]. Even if a feasible potential perturbation of 1% is assumed from its unperturbed equilibrium state during the SPI excitation, the numerical value of the perturbed potential ($\phi_1$) turns out to be 0.6 V. Using this

approximation yields a magnitude of ~0.03 V m of the involved constants $C$ and $c_2$. It is noteworthy that considering $C = c_2$ and $C \neq c_2$ produces two different potential characteristics as discussed in Fig. 4.1. While the case $C = c_2$ yields experimentally corroborating profiles [4, 5], the case $C \neq c_2$ yields some peakonic profiles not bolstered by any known experimental results. Considering the more relevant case of $C = c_2 = 0.03$ V m and $\gamma = 510$ m$^{-2}$ [13], the other constant $A$ ($= 2C\gamma^2$) is evaluated to be $1.56 \times 10^4$ V m$^{-3}$ from Eq. (4.35).

Having estimated the values of the relevant constants for potential perturbation, we substitute $\phi_1(r)$ from Eq. (4.34) in Eqs. (4.28)-(4.29), to get the perturbed electron and ion densities respectively as

$$n_{e1} = n_{ce1}\exp(-2\gamma r^2) + \left(F_e + \frac{G_e}{r}\right)\exp(-\gamma r^2) + \frac{H_e}{r} + L_e; \tag{4.36}$$

$$n_{i1} = n_{ci1}\exp(-2\gamma r^2) + \left(F_i + \frac{G_i}{r}\right)\exp(-\gamma r^2) + \frac{H_i}{r} + L_i; \tag{4.37}$$

Here,

$$n_{ce(i)1} = \pm\frac{3en_cA}{20\gamma k_BT_e}, \tag{4.38}$$

$$F_{e(i)} = \pm\frac{3en_cc_2}{10k_BT_e}, \tag{4.39}$$

$$G_{e(i)} = \pm\left(\frac{3en_cA}{40k_BT_e}\right)\sqrt{\frac{\pi}{\gamma}}, \tag{4.40}$$

$$H_{e(i)} = \pm\left(\frac{3en_cc_2}{20k_BT_e}\right)\sqrt{\frac{\pi}{\gamma}}, \tag{4.41}$$

$$L_{e(i)} = \left(\frac{3p_on_c^2}{10k_BT_e}\right)v_{e(i)c}. \tag{4.42}$$

Now, it is pertinent to figure out the magnitudes of the involved constants (Eqs. (4.38)-(4.42)) to study the characteristics of number densities through graphical analysis. The perturbed densities ($n_{e(i)1}$) in Eqs. (4.36)-(4.37) can be estimated from their corresponding equilibrium magnitudes ($n_{e(i)o}$). The magnitude of $n_{e(i)o}$ ranges between $10^{12}$ m$^{-3}$-$10^{17}$ m$^{-3}$ depending on the experimental arrangements [4, 5]. Hence, assuming a perturbation of less than 1% from the equilibrium number density (say, $n_{e(i)o} = 10^{12}$ m$^{-3}$), the perturbed density can be approximated to be $n_{e(i)1} \approx 10^8$ m$^{-3}$ during the SPI excitation.

Assuming some magnitudes of the leading constant, $n_{ce(i)1}$, such as $10^4$, $10^5$, and $10^6$ m$^{-3}$, in view of $n_{e(i)c}$, the other involved constants, viz., $F_{e(i)}$, $G_{e(i)}$, and $H_{e(i)}$ can be evaluated using the already derived $A$ and $C$ $(= c_2)$ values. The last constant $L_{e(i)}$ must also be empirically assumed due to the presence of unknown $v_{e(i)c}$ factor. This assumption does not qualitatively vary the nature of density perturbation. The number densities (electron and ion) can further be qualitatively analyzed by using these constants in relevant equations. The scale of perturbation is admitted varying from experimental reporting, however, the characteristics of spatial variation of the perturbation is conjectured to remain same, as all the involved constants are evaluated in conformity with each other and not randomly set.

Considering different values for $n_{e(i)c1}$ and $A$ $(= 2\gamma^2 C;\ C = 0.01 - 0.03$ V m) corresponds to different values of $en_c/k_BT_e$ from Eq. (4.38). These term values are further used in evaluating $F_{e(i)}$, $G_{e(i)}$ and $H_{e(i)}$. A table (Table 4.1) comprising of the various associated constants and their relative magnitudes according to the scale of perturbation is provided below to compare the strengths of the involved constants. The content in the table is used in generating respective plots for analyzing the results.

**Table 4.1: Empirically assumed and evaluated parameters for density perturbation**

| S. no. | $C = c_2$ (V m) | $A\ (= 2\gamma^2 C)$ (V m$^{-3}$) | $n_{ce(i)1}$ (m$^{-3}$) | $en_c/k_BT_e$ (C kg m$^{-3}$ s$^2$) | $F_{e(i)}$ (m$^{-3}$) | $G_{e(i)}$ (m$^{-2}$) | $H_{e(i)}$ (m$^{-2}$) | $L_{e(i)}$ (m$^{-3}$) |
|---|---|---|---|---|---|---|---|---|
| 1 | 0.01 | $5.20 \times 10^3$ | $10^5$ | $6.535 \times 10^4$ | $1.96 \times 10^2$ | $2 \times 10^6$ | 7.685 | $10^5$ |
| 2 | 0.02 | $1.04 \times 10^4$ | $10^6$ | $3.267 \times 10^5$ | $1.96 \times 10^3$ | $2 \times 10^7$ | 76.85 | $10^6$ |
| 3 | 0.03 | $1.56 \times 10^4$ | $10^4$ | $2.179 \times 10^3$ | $1.99 \times 10^5$ | $2 \times 10^5$ | 0.768 | $10^4$ |

Having evaluated the relevant constants for density perturbation, we, now derive the modified (perturbed) SPI driven electric field across the IFB with the negative gradient of the quasilinear electrostatic potential variation (Eq. (4.34)) given as

$$E_1(r) = -\partial_r \phi_1(r) = \frac{1}{r^2}(C\exp(-\gamma r^2) - c_2) + 2\gamma C\exp(-\gamma r^2). \quad (4.43)$$

The derived sets of quasilinear expressions, viz., electrostatic potential ($\phi_1$), electric field ($E_1$), electron (ion) velocity ($v_{e(i)}$), and electron (ion) number density ($n_{e(i)}$) are further elaborated with 2-D and 4-D plots using MATLAB tool. The plots manifest the excitation of the SPI with greater clarity across the radial distance relative to the center of the IFB within the paradigm of spherical symmetry.

## 4.3 RESULTS AND DICUSSIONS

A theoretical bifluidic plasma model is constructed herein to study the quasilinear SPI dynamics in an IFB system in laboratory plasmas. The basic governing equations are developed under the judicious approximation of spherically symmetric geometry. The applied quasilinear (first-order) perturbation technique reduces the SPI analysis into a linear ODE(2) with a set of unique variable coefficients of multiple orders (Eq. 4.30). The quasilinearly perturbed parameters, viz., particle velocity, electrostatic potential, charge number density, and electric field are numerically analyzed and graphically illustrated in feasible plasma parametric windows. The outcomes are bolstered by both experimental observations [13] and theoretical boundary conditions [7] in light of the literature.

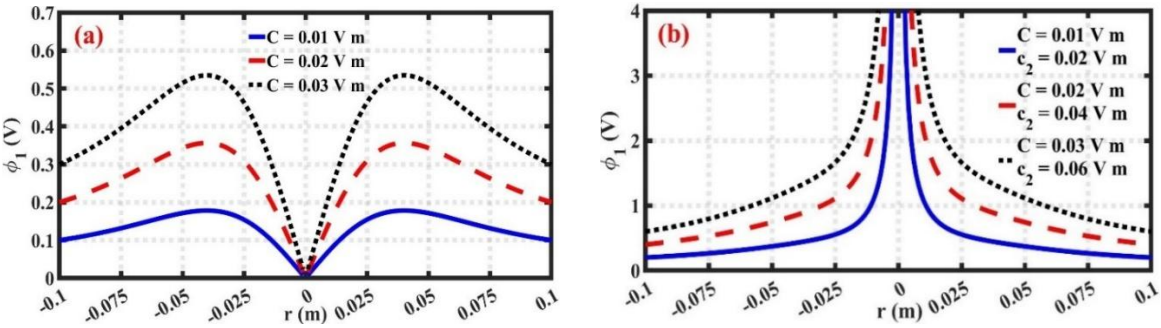


***Figure 4.1****: Profile of the perturbed potential across the IFB system (in SI units) with (a)* $C = c_2$ *(*$C = 0.03$ *(black dotted line),* $C = 0.02$ *(red dashed line),* $C = 0.01$ *(blue solid line)); and (b)* $C \neq c_2$ *(*$C = 0.03$*,* $c_2 = 0.06$ *(black dotted line);* $C = 0.02$*,* $c_2 = 0.04$ *(red dashed line);* $C = 0.01$*,* $c_2 = 0.02$ *(blue solid line)).*

The variation in the assumed values of the associated constants (e.g., $C$ and $c_2$ in $\phi_1$) yields variation in the derived plasma parameters. The numerical values of the integration constants are adopted in accordance with the experimental observations reported in the literature as already explained [4, 5]. Nevertheless, it is admitted that the numerically

derived plasma parameters may differ from their actual experimental magnitudes due to the assumed values of some of the associated constants encountered ahead.

The nature of the spatial variations of the numerically derived perturbed potential should be congruent with the corresponding experimental scenarios. The SPI excites across the sheath width (experimentally at $r \approx 0.10$ m for IFB) and the electrostatic potential is constant at the centre ($r = 0$) as the IFB anode acts as a Faraday cage. Thus, both constants ($C$ and $c_2$) in quasilinear potential expression are equated (in Fig. 4.1(a)) to yield $\phi_1(r = 0) = 0$. It results in an atypical bifold-solitonic perturbed potential profiles with no wave amplitude at the centre and an apparent standing wave-like (evanescent) behaviour in the off-centric regions. It is seen that the two distinct sets of the constants result in two separate scenarios of potential variations because of the parametric dependency of such nonlinear plasma problems on the adopted input-initial setup (Fig. 4.1).

The generated nonlinear potential patterns in a quasilinear treatment resemble the experimental observations reported in the literature [4-6]. These observations examine the SPI and SPR growth through reflection measurements from the anodes and RF probes. Some low-amplitude microwave radiation is projected on the oscillating sheath around the probes from the installed emitters and their temporal variations are noticed for various anode voltages. The reflection maxima, hence, the SPR and the SPI excited in the plasma-electrode system are investigated with this technique. The core reason for the excitation of the SPI is nonzero electron inertia and negative RF sheath resistance, as a field free cold plasma and electron depleted sheath behave as inductor and capacitor, respectively [4, 5].

The two different plots insinuate two unique spatial variation patterns of the perturbed potential. Therefore, two distinct conditions dictated by the involved constants are considered for our analysis in the purview of experimental results. It is to be highlighted that the apparent amplitudes of the perturbed parameters in the two figures pretend to substitute for each other having contrasting rise and fall. Here, Fig. 4.1(a) manifests a nonzero potential perturbation at the sheath region ($r \approx |0.08|$ m to $|0.10|$ m) and its convective migration inwards. The pulses of SPI disturbance generated at the sheath region moves inward convectively with every successive pulse. The successive pulses of SPI disturbance produced across the sheath feedback the previous pulse already moved ahead (towards the center) constructively in phase (amidst the sheath and center), as well as destructively out of phase (at the center), resulting in a spatial variation of the fluctuation amplitudes. The SPI disturbance created in the rarer sheath region propagates towards the

denser center region against the usual direction of quasi-equilibrium convective flow. So, the SPI disturbances gradually lose their velocity and magnitude while moving towards the center. Thus, every slowing pulse moved ahead is constructively feedbacked by the successive (faster) pulses approaching from behind (sheath region) at certain balancing distances (within $r \approx |0.03|$ m to $|0.05|$ m). It results in a more pronounced SPI disturbance in terms of the potential perturbation within that region amid the sheath and the IFB center. The fluctuation amplitude, however, diminishes towards the center due to the gradually increasing viscosity ($\xi(\propto n_{e(i)})$) because of the homogeneous charge number density ($n_o = n_c \exp(-\gamma r^2)$) having its peak value ($n_c$) at the center.

Whereas Fig. 4.1(b) offers a simpler view of the SPI. The instability disturbance originated at the enveloping sheath region migrates towards the center amidst the growing fluid density and positively feedback the instability amplitude centrally (at $r = 0$).

The first case with $C = c_2$ yields outcomes which corroborate with the experimental observations previously reported bifold-solitonic and standing wave-like (evanescent) spatial behavior. However, the second case with $C \neq c_2$ is a purely mathematical outcome. Although it is mathematically feasible and fulfils the boundary condition ($\phi_1(r \to \infty) = 0$) of extremum, this outcome certainly lacks any known experimental approval. However, the authors are unable to nullify any such SPI driven experimental reporting under special conditions of pressure, viscosity, density, etc. in IFB systems.

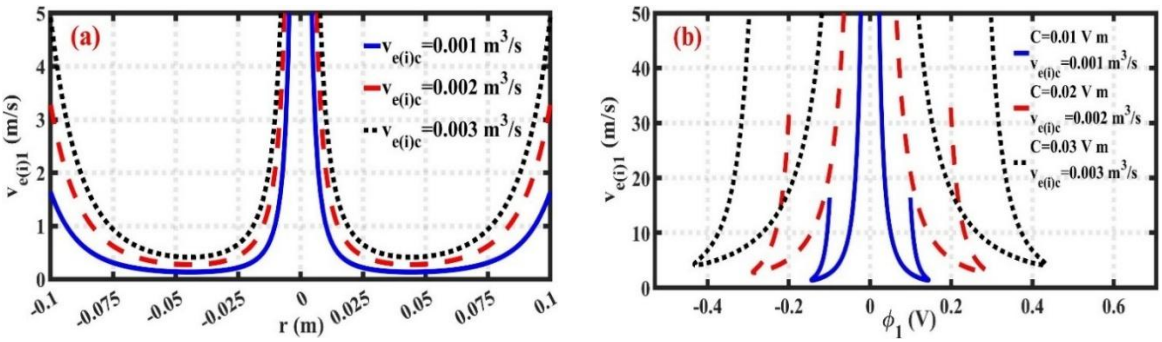


***Figure 4.2****: Profile of the quasilinear electron (ion) velocity ($v_{e(i)1}$) with variation in the (a) radius (r) relative to the IFB centre and (b) perturbed electrostatic potential ($\phi_1$) for different special cases dictated by the different velocity and potential integration constants given in the text.*

The distinct lines in Fig. 4.2(a) correspond to the different magnitudes (in SI units) of the integration constants appearing in the quasilinear velocity expressions as $v_{e(i)c} =$

$3 \times 10^{-3}$ (black dotted line), $v_{e(i)c} = 2 \times 10^{-3}$ (red dash-dotted line), and $v_{e(i)c} = 10^{-3}$ (blue solid line). The different lines in Fig. 4.2(b) link to the existent constants (in SI units) given as $C = c_2 = 0.03$, $v_{e(i)c} = 3 \times 10^{-3}$ (black dotted line); $C = c_2 = 0.02$, $v_{e(i)c} = 2 \times 10^{-3}$ (red dashed line); $C = c_2 = 0.01$, $v_{e(i)c} = 10^{-3}$ (blue solid line). It may be emphasized that there is no qualitative variation in the velocity due to any change in the magnitudes of the considered involved constants. The maxima and minima continue to form in their respective similar spatial distances.

There is a characteristic variation in the velocity perturbation across the IFB. This denotes acceleration and deceleration of the charge fluids due to the SPI excitation across the sheath region. These profiles display the atypical characteristic outcome of the SPI excited in an IFB system expressed in terms of the velocity perturbation. The apparent spike in velocity beside the sheath region ($r \approx |0.08|$ m) denotes the SPI-induced acceleration of the charged fluids due to the oscillating sheath during the SPR. But, because of the potential perturbation, bulk viscosity, equilibrium density, and other possible agents acting as resistive factors in the medium, a subsequent fall in the velocity perturbation is noticed amidst the sheath and the center (within $r \approx |0.06|$ m to $|0.04|$ m). This also insinuates the fluids drifting towards their unperturbed equilibrium velocity magnitudes due to reduction in their perturbation scale. However, the subsequent pulses of velocity from the sheath reaches and accelerates the fluid through convection with an apparent rise just beside the IFB center. The more pronounced potential perturbation in the intermediate region (in between the sheath and IFB center) results in a reduction in the velocity perturbation across that region (Fig. 4.2(a)-4.2(b)). The potential perturbation is hence observed to act as a resistive factor to fluid velocity. The same may also be noticed from Fig. 4.3(a) that respective maxima and minima of potential and velocity perturbations coexist spatially. In brief, the successive pulses of velocity perturbation feedback each other forming variations in magnitudes due to the nonlinear fluid convection and linear fluid dispersion (in small scale) resulting in the evident quasilinearity.

The spatial variation of the velocity perturbation (Fig. 4.2(a)) can be explained with the potential perturbation (Fig. 4.1(a)). The electronic and ionic fluids acquire a sudden high velocity near the sheath due to the excited SPI but gradually decay with the higher density of the fluid towards the center. The successive hike in the velocity perturbation is due to the feedback from the propagatory nature of the instability.

It is clearly shown in Fig. 4.3 that the profiles of the (a) potential (solid lines) and electron (ion) velocity (dotted lines) along the same y-axis with variation in radius along x-axis, relative to the IFB center and (b) the same velocity with variation in the plasma electric field. The various potential curves (solid lines) and velocity curves (dotted lines) in Fig. 4.3(a) correspond to $C = c_2 = 0.03$ (black solid line), 0.02 (red solid line), 0.01 (blue solid line), $v_{e(i)c} = 3 \times 10^{-4}$ (black dotted line), $2 \times 10^{-4}$ (red dotted line), $10^{-4}$ (blue dotted line); respectively. Similarly, the different velocity curves in Fig. 4.3(b) link to $C = c_2 = 0.03$, $v_{e(i)c} = 3 \times 10^{-3}$ (black dotted line); 0.02, $2 \times 10^{-3}$ (red dashed line); and 0.01, $10^{-3}$ (blue solid line) (in SI units).

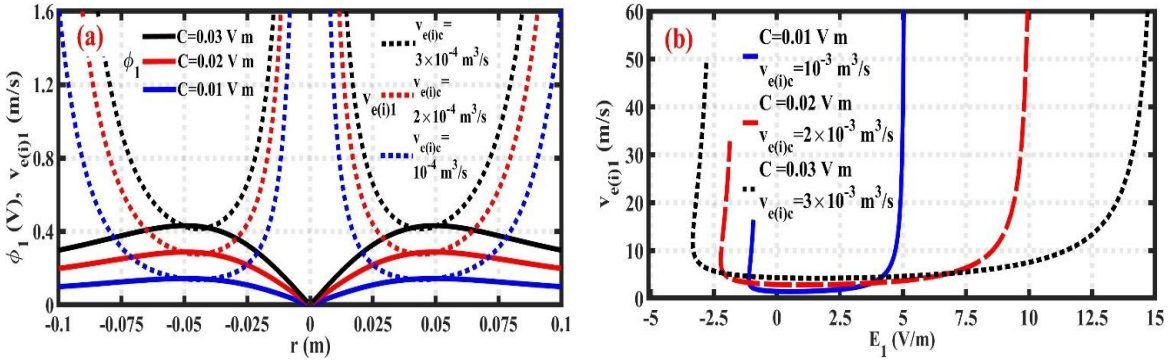


***Figure 4.3****: Profile of the (a) velocity ($v_{e(i)1}$) of the electron (ion) fluid (dotted lines) and potential ($\phi_1$) (solid lines) with variation in the radius ($r$) relative to the IFB center and (b) velocity ($v_{e(i)1}$) with variation in the associated electric field ($E_1$) for different integrated special cases of potential and velocity.*

Two different electric field strengths with opposite polarities evidently yield charge fluid velocity of the same magnitude (Fig. 4.3(b)). The magnitudes of the involved constants ($C$, $c_2$, and $v_{e(i)c}$) are assumed as per a suitable compatibility condition on the same graphical footing judiciously. The apparent asymmetry of the velocity curves across the field polarity reversal ($-E_1$ to $+E_1$) is an outcome of the experimentally observed nonzero inertia of the electronic fluid (during high-frequency SPI). The charged fluids fail to respond to the fast-changing polarity of the field ($E_1$) instantaneously. In case of a zero-inertia fluid, it would form a symmetric curve of the velocity across the region $E_1 = 0$, as the velocity of the charged fluids could immediately change its direction across the IFB center ($r = 0$) and acquire the same velocity magnitude with the same field strength, but with an opposite polarity ($-E_1$ or $E_1$).

It may further be explained as the ambient plasma electrons passing through the tiny holes on the IFB electrode surface and accumulating at its centre during the positive field polarity ($E_1 > 0$). This dominant electronic movement results in the charged fluid velocity ($v_{e(i)1}$) noticed during the $E_1 > 0$. The electrostatic potential difference generated due to these accumulated electrons intends to disperse them outwards to attain an equilibrium when the field polarity tends to neutralize ($E_1 \to 0$). Although the accumulated electrons could disperse outwards during $E_1 \sim 0$, but their inertial nature delays their outward movement. The accumulated electrons disseminate outwards belated and again a positive $v_{e(i)1}$ is noticed at $E_1 < 0$, but this time against the electrode field polarity and showing a different (steeper) $v_{e(i)1}$ characteristic than shown at the $E_1 > 0$. This inertia is an outcome of the high-frequency field polarity fluctuation during the SPI excitation. Therefore, it is evident that the bifluidic plasma model corroborates with the experimentally reported inertial behavior of the charges (at SPI onset) as found in the previous findings [4-6].

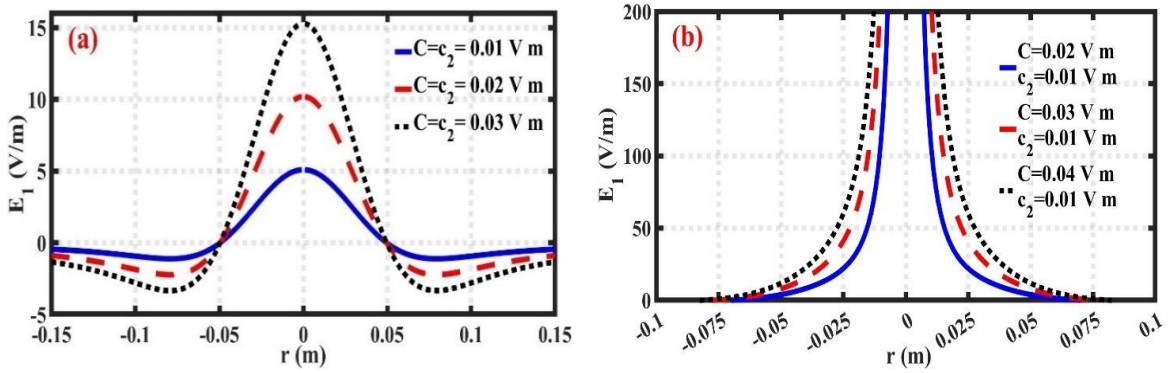


***Figure 4.4****: Profile of the electric field with variation in the radius relative to the IFB center for the associated constants in two distinct cases indicated with (a) equal magnitudes and (b) unequal magnitudes.*

We highlight the quasilinear spatial variation of electric field ($E_1$) with two different constants ($C$ and $c_2$) in two separate cases (in Fig. 4.4) having (a) equal values (0.03 (black dotted line); 0.02 (red dashed line); 0.01 (blue solid line)) and (b) unequal values ($C = 0.04$, $c_2 = 0.01$ (black dotted line); 0.03, 0.01 (red dash-dotted line); and 0.03, 0.01 (blue solid line)), respectively. The nature and magnitude of the perturbed electric field is found to vary with the varying magnitudes of the associated constants. A fall in the field perturbation is noticed in the region between the sheath and IFB center (within $r \approx 0.10$ m to $r \approx 0$) with a successive rise towards the center. It may be noteworthy that Figs. 4.4(a)-

4.4(b) also manifest the rate of spatial variations of the previous potential perturbations already shown in Figs. 4.1(a)-4.1(b), respectively. The quasilinear field profiles account for the force exerted ($F(= eE)$) on the charged fluids due to the SPI-induced perturbations. An increase or decrease in the field perturbations results in a change in the acceleration of the charged fluids. Such field variations result in a congruent velocity variation as manifested in Fig. 4.2. The derived quasilinear plasma parameters consistently corroborate with each other proving efficacy of the bifluidic PFS analysis for the SPI study in such IFB systems.

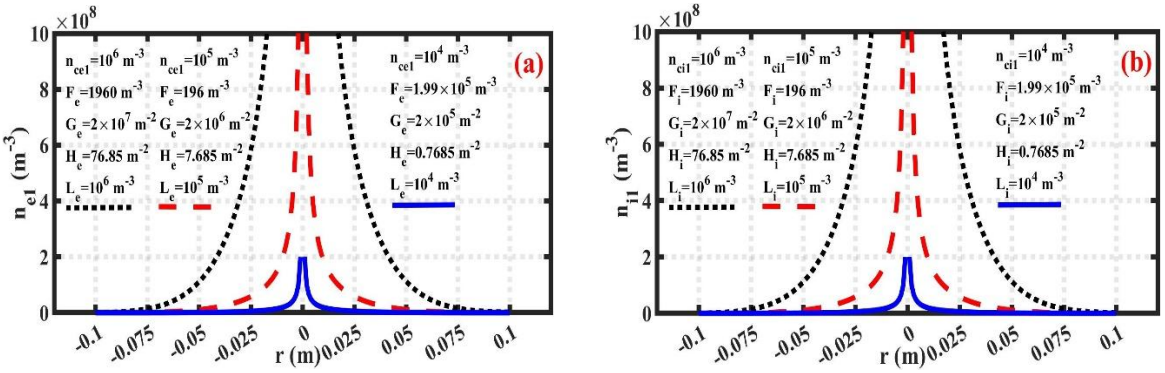


***Figure 4.5****: Profile of the (a) electron densities and (b) ion densities with variation in the radius.*

The density perturbation is noticed to be most pronounced (peaky) at the IFB center (at $r = 0$). The associated constants are used from table 4.1. The various lines correspond to different relative values of the associated constants (in SI unit), viz., $n_{ce(i)1} = 10^4$, $F_{e(i)} = 1.99 \times 10^5$, $G_{e(i)} = 2 \times 10^5$, $H_{e(i)} = 0.7685$, $L_{e(i)} = 10^4$ (blue solid line); $10^5$, $1.96 \times 10^2$, $2 \times 10^6$, 7.685, $10^5$ (red dashed line); $10^6$, $1.96 \times 10^3$, $2 \times 10^7$, 76.85, $10^6$ (black dotted line). The quasilinear density perturbation of both the electron and ion manifests a spike at the IFB center. This characteristic rise authenticates the experimentally reported homogeneous density ($n_{e(i)o}$) variation of gaussian nature ($n_{e(i)} = n_c \exp(-\gamma r^2)$) with a peak ($n_c$) at the IFB centre. The greater density perturbation at the centre is a consequence of the collective perturbation of electrostatic potential ($\phi_1$), electric field ($E_1$), velocity ($v_{e(i)1}$), and the convective transfer of disturbance from the outermost sheath to the core. Hence, it may also be conferred that the free energy required to excite the plasma instabilities is a yield of the steep charge number density gradient across the sheath in both the distinct classes of FBs, i.e., the regular fireballs (RFBs) and the IFBs.

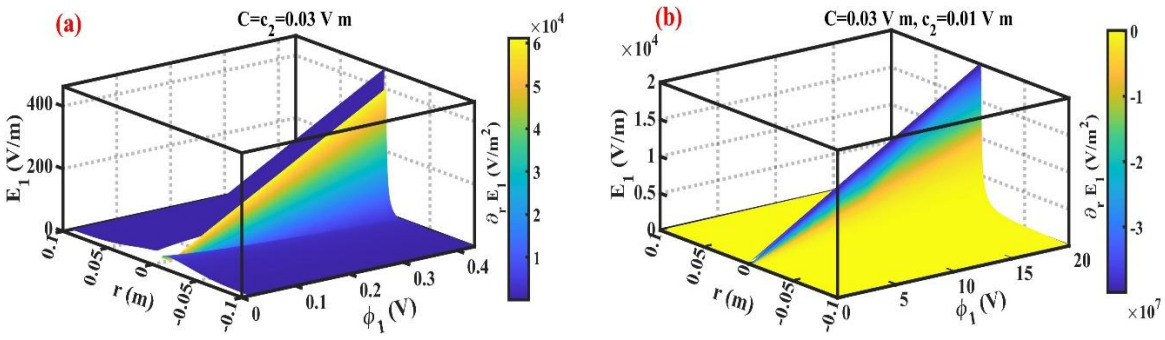


***Figure 4.6**: Colormap (4-D) profile of the electrostatic potential ($\phi_1$), electric field ($E_1 = -\partial_r \phi_1$), and potential curvature ($\partial_r E_1$) with variation in the radius ($r$) relative to the IFB center for (a) equal and (b) unequal magnitudes of associated constants (in SI units).*

The changes in color gradient in the adjacent color bars denote the spatial rate of change of the electric field. The colormaps (a) and (b) correspond to two associated constants (in SI unit) with different assumed magnitudes in an equal ($C = c_2 = 0.03$) and unequal ($C\ (= 0.03) > c_2 (= 0.01)$) footings, respectively. The 4-D colormaps in Fig. 4.6 validate 2-D plots shown of Fig. 4.4 for respective values of the constants ($C$ and $c_2$). The similar standing wave-like nature of the field disturbance is manifested for $C = c_2 = 0.03$ configuration. As no field perturbation is noticed outside the IFB radius ($r \approx 0.10$ m) due to instability reflection from the sheath. Besides, the same peakon-type field perturbation is also noticed for $C = 0.03$; $c_2 = 0.01$ ($C \neq c_2$) configuration with minimum (negative) potential curvature at the center. It is noteworthy that, with both the configurations of the constants, there is an apparent central spike of field perturbation (positive or negative) at $r \approx 0$. It proves the convective migration of the SPI disturbance generated at the IFB sheath towards its center in both the cases ($C = c_2$ and $C \neq c_2$). It should, hence, be added that the 4-D colormaps corroborate with the previous 2-D potential profiles (Fig. 4.1) and electric field profiles (Fig. 4.4) emboldening the outcomes consequent on the quasilinear IFB perturbation analysis proposed herein.

It is evidently proven from Fig. 4.7(a) (as in Fig. 4.3(a)) that an increase in the electrostatic potential ($\phi_1$) reduces the velocity ($v_{e(i)1}$), and vice-versa. Hence, an out-of-phase behavior is witnessed in between these two parameters, as experimentally reported previously [4-6]. It is further seen that the same value of electronic (ionic) fluid velocity ($v_{e(i)1}$) yields two different values of the electric field ($E_1$) (Fig. 4.3(b)). This hysteretic behavior is a result of the nonzero electron inertia at the high frequency (in GHz range) SPI instigated in the IFB system. The inertial electrons (at SPI frequency) fail to immediately

respond to the changing polarity of the electrostatic potential ($\phi_1$) without a substantial phase difference. Instead, the two parameters differ by a phase of 180°.

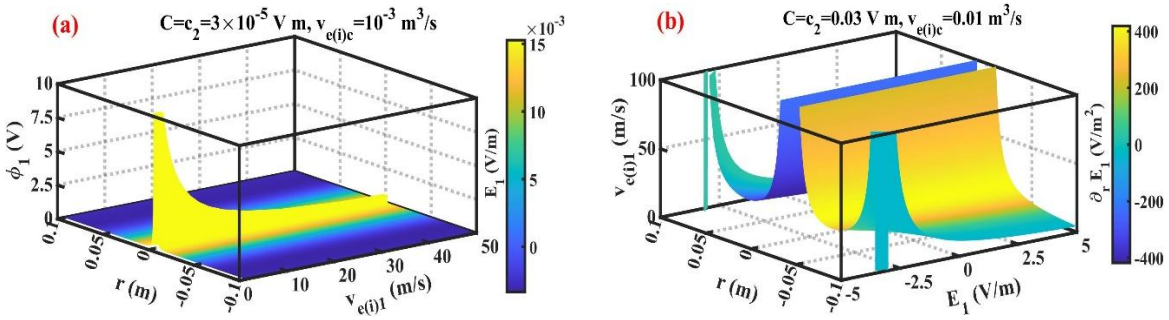


***Figure 4.7****: Colormap (4-D) profiling the conjoint spatial variation (with $r$) of (a) velocity ($v_{e(i)1}$), electrostatic potential ($\phi_1$), electric field ($E_1$) for $C = c_2 = 3 \times 10^{-5}$, $v_{e(i)c} = 10^{-3}$; and (b) velocity ($v_{e(i)1}$), electric field ($E_1$), potential curvature ($\partial_r E_1$) for $C = c_2 = 0.03$, $v_{e(i)c} = 0.01$ (in SI units).*

The same inertia induced velocity, potential, and field correlation in the charge fluid movement can also be observed across the 4-D colormap profiles in Fig. 4.7. It may also be observed from colormap in Fig. 4.7(b) that same velocity magnitude corresponds to different electric field strengths with asymmetric variation. The color gradient in Fig. 4.7(b) denotes significant potential curvature during the SPI. As a result, a significant rate of force variation is experienced by the charge fluids. Similarly, in Fig. 4.7(a), a substantial color gradient (electric field strength) is apparent through the color bar. This reflects a steep variation in the electric field ($E_1$) strength, and thus also the force experienced by the charged fluids with their spatially varying velocity ($v_{e(i)1}$) (along x-axis) due to the excited SPI across the IFB system. This effectively proves the experimentally reported electron inertia, phase difference during electronic oscillation, standing-wave like behavior, etc.

## 4.4 CONCLUSIONS

The SPI-induced fluctuation dynamics across an IFB system in bounded bifluidic plasmas is studied through a methodically developed quasilinear model formalism on relevant laboratory scale. A unique class of peakonic and bifold-solitonic structures is found to be excited in the form of electrostatic potential and electric field across the IFB sphere. These bifold-solitonic structures originate due to the reflection of the SPR pulses from the sheath boundary, re-structuring them into bifold-solitonic profiles. The bifold-solitonic profiles

with mathematical expressions $\{\exp(-\gamma r^2) - 1\}/r$ differ against the conventional ion-acoustic solitons mathematically expressed as $\mathrm{sech}^2\{(r - vt)/L\}$, here, $v$ and $L$ denote soliton velocity and soliton length, respectively [7].

The graphical profiles of the quasilinearly perturbed physical parameters corroborate with each other with feasible physical explanations on applying relevant boundary conditions (zero magnitude at infinity) [7]. In addition, a smooth triangulation of electrostatic potential ($\phi$), field ($E$), velocity ($v_{e(i)}$), and potential curvature ($\partial_r E$) yields a new spectral variety of 4-D colormaps formed by the derived parameters (Figs. 4.6-4.7). These spatiospectral colormaps manifest a collective variation of the associated plasma parameters with respect to each other along with variation in the radius relative to the IFB center. This model analysis is effective in reproducing multiple experimental results, as previously reported [4, 5], on the multi-parametric perturbation characteristics in accordance with those noticed herein.

The quasilinear perturbation analysis done herein reduces the SPI-driven IFB system dynamics to a unique class of linear ODE(2) with multi-parametric variable coefficients. In other words, these ODEs vary with the involved dependent parameters, such as the constitutive velocity, electrostatic potential, and electric charge density fields. The nonzero perturbed parameters with their increasing magnitudes in different conditions manifest a substantial strength of the SPI excitation across the IFB sheath and DL structures. The nature of the derived and modified quasilinear expressions is analyzed illustratively. It corroborates fairly with the previously reported results in similar IFB configurations [9, 11]. It may be conjectured herewith that the proposed SPI analysis offers a theoretical stand to understand the experimentally witnessed results. Besides, the resemblance of peakonic profiles of the current work with those previously reported in the quasilinear [9] and higher-order PFS analyses [11] further emboldens the proposed analysis. The atypical bifold-solitonic potential structures (Fig. 4.1(a)) go congruent with the experimentally reported standing wave-like (evanescent) profiles [6]. However, a few of the quasilinear parametric variations, as observed herein, are yet to be well-studied experimentally. Thus, the reliability of this quasilinear analysis can be well judged on the grounds of diversified plasma parametric scenarios experimentally reported earlier.

It may be pertinent to mention that the instigation of an instability (e.g., SPI) in a plasma system may trigger other possible closely correlated instabilities portraying plasma restructuration in different conditions. Besides, some of the plasma instabilities, dominant

in other plasma systems in addition to the SPI, may also excite in IFB systems [2]. This broader classification includes the Rayleigh-Taylor instability (RTI), relevant in supernova explosion, tokamak, solar corona, volcanic eruption, etc. [14]. The Kelvin-Helmholtz instability (KHI) is highly relevant in oceanic environments [15], molecular clouds and atmospheric sciences [16], etc. The two-stream instability (TSI), relevant in protoplanetary disks [17], the potential relaxation instability (PRI), sensible in plasma probe diagnostics [18], and so forth. Therefore, theoretical modelling of an IFB system finds its pertinence in a broader instability horizon reflecting an enormous potential of naturalistic applicability.

It is pretty evident that the SPI analysis in an IFB system can efficaciously find its diversified applications in multiple plasma processing systems, alongside other collective instabilities of applied value in various astroplasmic, cosmoplasmic, and space-laboratory scenarios. The IFB research is applicable in several realistic sectors of remarkable technological relevance as follows:

(i) In isotope collection: The plasma is heated through ion cyclotron resonance technique. The various plasma constituents due to their mass (M) differences acquire different frequency of oscillation to the applied RF electric field through the plasma submerged anodes. With an application of homogeneous magnetic field (B) the cyclotron frequency reaches a magnitude of $\Omega = qB/Mc$, where $q$ and $c$ are the magnitudes of isotopic charges and light velocity in vacuum, respectively. The physical separation created due to the mass difference of the isotopes oscillating at different frequencies helps in collecting them through various technical arrangements. In plasma FB systems, the collection occurs through electrodes set at different potentials [19]. The spatial variation of potential, electric field, density, and velocity across the electrodes due to excited SPI analyzed here can be useful in designing and managing the system accordingly for efficient isotopic collection. The instantaneous presence of the isotopes can be judged more accurately with the outcomes of this IFB research. It hereby provides the applicability of the IFB research in isotope collection techniques, further useful in medical and defense applications.

(ii) Spacecraft antenna signal processing: The SPI analysis herein is useful in analyzing antenna signals received from the spacecrafts, as the antennas get charged in the

astroplasmic environs and formation of enveloping plasma sheaths due to the SPI excitations consequent on the applied potential variations [4].

Besides, the electrons trapped in the vicinity (cavity field) of an anode (e.g., an antenna in astroplasma) and oscillating at certain frequency can release a burst of MW range radiation. A similar cavity resonance can also occur in an IFB arrangement when the electrons move to-and-fro across the IFB anode during the SPI excitation. The study of SPI and the associated SPR [4] is useful in understanding MW radiation generated through an obitron maser device (an instrument used to amplify and generate coherent monochromatic EM radiation in MW range by excited atoms) [20].

(iii) Ultra-relativistic GRBs: The neutron stars and blackholes emanate shock waves propagating at ultra-relativistic speeds. The consecutive shockwaves moving outward relative to their origins gradually get slower and start inter-shock interactions. Such inter-shock interactions eventually lead to the formation of GRBs followed by afterglows. Such astronomical event resembles that of an electric potential and field perturbation behavior in an IFB formation in laboratory plasma scenarios (Figs. 4.1, 4.4). The central anode upon having a variable biasing emanates shocks and bursts of similar kind [3]. It is found through the analysis of IFB that the disturbance generated at the center moves outwards gradually reducing its speeds. Hence, different consecutive disturbances moving outwards manage to interact at certain distances forming maxima of disturbance, resembling that of the shock waves associated with GRBs. Therefore, the laboratory FB models could be extensively helpful in modelling astronomical GRBs simulatively. Thus, two distinct FB events, viz., in laboratory scales and in astronomical scales of space and time, can be well-addressed with the scale-invariant physical insights of usual small-scale plasma FB models [10, 21].

(iv) Magnetar energy emission: Magnetars are strongly magnetized neutron stars with extremely high magnetic field ($\sim 10^{14} - 10^{15}$ G). They release their energy through the field re-structurization followed by consequent sporadic X-ray bursts [22]. The X-ray bursts are classified into three categories based upon the magnitudes of their energy release. The weaker and intermediate bursts are prevented by the magnetosphere region, whereas the strong bursts stream through it. The prevented bursts rather cool gradually though radiation. The FB forms because of the magnetosphere blocking

small intensity bursts. The high radiation pressure expels plasma from inside [22]. Some properties of the magnetars include the presence of a baryon loaded sheath which prevents incessant passage of radiation from it outward to the interstellar medium and allows only partial evaporation of matter. This sheath also prevents the ablation of material from the magnetars. In terms of geometry, both the IFB and magnetars behave apparently the same as the central FB enclosed by an encompassing spherical sheath [23]. Therefore, the dynamics of the magnetars and their baryon-loaded sheaths play similar roles in their stability as that of IFB systems encompassed by their sheaths as formed in laboratory plasma chambers.

In addition, the radiation hydrodynamic pressure generated beneath the magnetized baryon-loaded sheath makes the evaporated matter accumulate around the magnetospheric regions of the magnetars. The accumulated matter remains levitated in the magnetospheric regions due to the radiation pressure reaching from the center of the FB. The formation of baryonic plasma within the magnetar (an astronomical FB) is, however, atypical to the astroplasma domains [22].

(v) Off-SPI instabilities: Various additional plasma instabilities, such as the two-stream, the Rayleigh-Taylor, the Kelvin-Helmholtz instabilities, and so forth, can be analyzed with the FB model, since a FB incorporates required electronic and ionic motions [3]. The already mentioned individual instability dynamics and their relationship with the FB formation are further illustrated below.

Two-stream instability (TSI): The intra- or inter-component charge particles having nonzero relative velocity may instigate the two-stream instability. In the case of a plasma FB, the streaming electrons, due to the anodic electric field, while interacting with considerably static thermal plasma electrons and ions, may deliver their energy to them, thereby increasing the wave amplitude excited by their relative motion. The exponential increase of the wave amplitude (if any) with respect to time, due to energy transfer from the stream to the wave is termed as the Two-stream instability (TSI). The relative velocity of the streaming electrons must be greater than or equal to the phase velocity of the small amplitude wave of the background plasmas. If this condition is not fulfilled, then it leads to wave damping, as the small amplitude wave then offers its own energy to the streaming charges (beam) [7].

Rayleigh Taylor instability (RTI): The fluid density gradient across the sheath and the presheath region around a plasma FB electrode provides a suitable ground for the excitation of the Rayleigh Taylor instability (RTI) in the presence of an electrode (central) electric field. This electric field pierces through the sheath and reaches the pre-sheath region. The sheath cannot completely enclose the electric field passing through it in case of a strong perturbation. This leaking electric field subsequently acts as 'effective gravity'. The charge number density in the sheath region is less than that in the pre-sheath and ambient plasma region. Therefore, the sheath and pre-sheath regions behave as lighter and heavier fluids, respectively. The heavier (pre-sheath) fluid rests upon lighter (sheath) fluid. The attained 'top-heavy' equilibrium once disturbed due to some perturbation makes the pre-sheath (heavy fluid) pierce through the sheath (lighter) region instigating the RTI with mixing of the two fluids due to the free energy [24].

The study of the RTI through the plasma FB model is also useful in astrophysical scenarios on a similar plasmic footing. The 3-D magnetohydrodynamic (MHD) simulations and successive observational results on solar up flows confirm them to be the RTI-centric unstable. Besides, the back falling of the plasma due to a failed coronal mass ejections (CMEs) show an RTI morphology [25]. Such back fallings can also be noticed in laboratory plasma FB sheaths, where electrons (ions) back fall for cathode (anode) at the FB center [26]. Similar evidence is also witnessed in the Sun (another FB) involving the RTI dynamics which are similar with laboratory plasma FB under study. The plasma FB model, hence, also helps in analyzing the RTI in solar atmosphere simulatively [24, 25].

Kelvin-Helmholtz instability (KHI): Two streams of fluids moving at different speeds may kick in the Kelvin-Helmholtz instability (KHI) excitation. In laboratory plasmas, the two streams of constituent fluids comprised of electrons and ions differ in terms of speeds and directions of movement across the FB system due to their different masses and charge polarities. With any perturbation in the system (across the streams), there appears some shrinks and expansions within the two laminar streams of the fluids. The fluids, due to Bernoulli's principle, intend to maintain the same rate of flow through these volumetric variations. Consequently, the regions with slower (expanded) and faster (shrunk) fluid speeds start to deform further. These deformations (curves spiraling) start to grow across the streams, gradually forming the KHI. The shear fluid

velocity threshold should be high enough to overcome the restraining surface tension force for the KHI excitation [27].

The KHI is also observed in the coronal mass ejection (CME), heliospheric and magnetospheric boundaries, cometary tails, astrophysical jets in the active galactic nuclei, and so on [28]. The reason for the KHI excitation continues to remain the same due to the presence of shear among the different density fluids. In the Sun, the interaction of denser ejecta lifted off from the solar surface and less dense coronal background triggers the KHI. Since Sun is also an astronomic FB, the laboratory FB model is useful in analyzing the KHI and its various outcomes in solar atmosphere proving the significance of IFB research through FB model.

(vi) Meteoritic radio afterglow (MRA): The meteoritic radio afterglows (MRAs) are produced intrinsically in the meteors [29]. Several MRAs are and some are also reflected by the meteor tails (coming from various stars) [30]. Such afterglows are termed MRAs. These MRAs form astronomical FBs [31, 32]. There are two hypotheses of the radiation mechanism of MRAs; one is the electrostatic plasma oscillations converting to EM radiation within the plasma tail (Langmuir wave) and the other being the resonant transition radiation (RTR). In the RTR, which occurs like that of Cherenkov radiation, the hot electrons while moving through a turbulent system can radiate due to changing refractive index (due to density variation also) with position [29]. The meteors are known to form astronomic FBs, and the established FB model also holds for the MRAs [31, 32]. It proves the relevance of laboratory FB research providing a simulative exploration for the MRAs through this bifluidic plasma model.

The proposed study could have several future applicability and scope in more sophisticated realistic scenarios in organically correlated directions in addition to the above. A few applications are already enumerated across the environment. Apart from the quasilinear SPI treatment as above, a similar follow-up formalism may hopefully be studied in less sophisticated (harmonically linear) and more sophisticated (anharmonically nonlinear) model frameworks in the future. The solitary wave patterns here can also be further explored in higher dimensions in more refined configurations with the help of nonlocal nonlinear perturbative analyses, with properly constructed stretched coordinates, well compatible with the diverse observational scenarios [33].

## REFERENCES

[1] Vanraes, P. and Bogaerts, A. The essential role of the plasma sheath in plasma–liquid interaction and its applications-A perspective. *J. Appl. Phys.*, 129(22):220901(1-37), 2021.

[2] Stenzel, R. L., Ionita, C., Scrittwieser, R. Plasma fireballs. *IEEE Trans. Plasma Sci.*, 36(4):1000-1001, 2008.

[3] Stenzel, R. L., et al. Sheaths and double layers with instabilities. *J. Technol. Space Plasmas*, 2(1):70-91, 2021.

[4] Stenzel, R. L. Instability of sheath-plasma resonance. *Phys. Rev. Lett.*, 60(8):704-707, 1988.

[5] Stenzel, R. L. High-frequency instability of the sheath-plasma resonance. *Phys. Fluids: Plasma Phys.*, 1(11):2273-2282, 1989.

[6] Stenzel, R. L., Gruenwald, J., Ionita, C., and Schrittwieser, R. Electron-rich sheath dynamics. I. Transient currents and sheath plasma instabilities. *Phys. Plasmas*, 18(6):062112(1-9), 2011.

[7] Chen, F. F., *Introduction to plasma physics and controlled fusion*, New York: Plenum Press; 1984.

[8] Vedenov, A. A. Quasi-linear plasma theory (theory of a weakly turbulent plasma). *J. Nucl. Energy, Part C Plasma Phys.*, 5(3):169-186, 1963.

[9] Dutta, S. and Karmakar, P. K. Fireball sheath instability. *J. Astron. Astrophys.*, 43(64):1-8, 2022.

[10] Waxman, E. Angular size and emission time scales of relativistic fireballs. *ApJ.*, 491(1):L19-L22, 1997.

[11] Dutta, S. and Karmakar, P. K. A Multi-Order Nonlinear Meta-Analysis of Bifluidic Fireball Sheath Fluctuations. *Waves Random Complex Media*, https://doi.org/10.1080/17455030.2023.2178826 2023.

[12] Wang, Y., and Du, J. The viscosity of charged particles in the weakly ionized plasma with power-law distributions. *Phys. Plasmas*, 25(6):062309(1-8), 2018.

[13] Gruenwald, J. On the dispersion relation of the transit time instability in inverted fireballs. *Phys. Plasmas*, 21(8):082109(1-5), 2014.

[14] Wani, R., et al., Rayleigh–Taylor instability in strongly coupled plasma. *Sci. Rep.*, 12(11557):1-13, 2022.

[15] Smyth, W. D. and Moum, J. N. Ocean mixing by Kelvin-Helmholtz instability. *Oceanography*, 25(2):140–149, 2012.

[16] Drazin, P. G. Dynamical Meteorology | Kelvin-Helmholtz instability. *Encyclopedia of Atmospheric Sciences*, 2:343-346, 2015.

[17] Youdin, A. N. and Goodman, J. Streaming instabilities in protoplanetary disks. *Astrophys. J.*, 620(1):459-469, 2001.

[18] Desjardins, T. R. and Gilmore, M. The potential relaxation instability in a helicon plasma. *Phys. Plasmas*, 25(6):062117, 2018.

[19] Dawson, J., et al., Isotope separation in plasmas by use of ion cyclotron resonance. *Phys. Rev. Lett.*, 37(23):1547, 1976.

[20] Alexeff, I. and Dyer, F. Millimeter microwave emission from a maser by use of plasma-produced electrons orbiting a positively charged wire. *Phys. Rev. Lett.*, 45(5):351-354, 1980.

[21] Ralph, A., et al., Shocked by GRB 970228: the afterglow of a cosmological fireball. *MNRAS*, 288(4):L51-L56, 1997.

[22] Demidov, I. and Lyubarsky, Y. Radiatively driven evaporation from magnetar's surface. *MNRAS*, 518(1):810-820, 2023.

[23] Gruenwald, J., Reynvaan, J. and Knoll, P. Creation and characterization of inverted fireballs in $H_2$ plasma. *Phys. Scr.*, T61(014006):1-3, 2014. [30]

[24] Pandey, B. P. and Roy, S. An explanation of the sheath plasma instability. *Phys. Plasmas*, 10(1):5-8, 2003.

[25] Carlyle, J. and Hiller, A. The non-linear growth of the magnetic Rayleigh-Taylor instability. *Astron. Astrophys.*, 605(A101):1-10, 2017.

[26] Chopra, N. S., et al., Determination of positive anode sheath in anodic carbon arc for synthesis of nanomaterials. *J. Phys. D: Appl. Phys.*, 55(114001):1-20, 2022.

[27] Masson, A. and Nykyri, K. Kelvin-Helmholtz instability: Lessons learned and ways forward. *Space Sci. Rev.*, 214(71):1-18, 2018.

[28] Foullon, C., et al. Magnetic Kelvin–Helmholtz instability at the sun. *ApJ Lett.*, 729(L8):1-4, 2011.

[29] Varghese, S. S., et al. Spatially resolved observations of meteor radio afterglows with the OVRO-LWA. *Journal of Geophysical Research: Space Physics*, 129(2): e2023JA032272, 2024.

[30] Zhao, F., et al. The intensity of diffuse galactic emission reflected by meteor trails. *MNRAS*, 527(2):4140-4152, 2024.

[31] https://www.imo.net/definitions-of-terms-in-meteor-astronomy-iau/

[32] https://cneos.jpl.nasa.gov/fireballs/intro.html

[33] Mahmood, S. and Ur-Rahman, H. Existence and propagation characteristics of ion-acoustic Kadomtsev–Petviashvili (KP) solitons in nonthermal multi-ion plasmas with kappa distributed electrons. *Chaos Soliton Fractals*, 169(113225):1-16, 2023.